

Electronic Supplementary Material (ESI) for Energy & Environmental Science. This journal is © The Royal Society of Chemistry 2025

Supplementary Information

Enhanced redox kinetics for hydrogen peroxide photosynthesis in high-concentration by encapsulating porphyrin metal–organic frameworks with phenolic resin

Houwei He,^a Zhongliao Wang,^a Jinfeng Zhang,^a Shavkat Mamatkulov,^b Olim Ruzimuradov,^b Kai Dai,^{*a} Jingxiang Low^{*c} and Yue Li^{*c}

^a Key Laboratory of Green and Precise Synthetic Chemistry and Applications, Ministry of Education, Anhui Province Key Laboratory of Pollutant Sensitive Materials and Environmental Remediation, School of Physics and Electronic Information, Huaibei Normal University, Huaibei 235000, P. R. China. E-mail: daikai940@chnu.edu.cn

^b Department of Natural-Mathematical Science, Turin Polytechnic University in Tashkent, Tashkent 100095, Uzbekistan

^c School of Physical Science and Technology, Tiangong University, Tianjin 300387, P. R. China. E-mail: jxlow@tiangong.edu.cn, yueli@issp.ac.cn

Experimental section

Materials. 4,4',4'',4'''-(Porphine-5,10,15,20-tetrayl) tetrakis (benzoic acid) (H₂TCPP), hafnium (IV) chloride (HfCl₄), benzoic acid (C₇H₆O₂), *N,N*-dimethylformamide (DMF), 3-aminophenol (C₆H₇NO), formaldehyde aqueous solution (CH₂O, 37–40 wt%), ammonia aqueous solution (NH₃·H₂O, 25–28 wt%), silver nitrate (AgNO₃), benzoquinone (BQ), 5,5-dimethyl-1-pyrroline N-oxide (DMPO), potassium titanium oxide oxalate dihydrate (C₄K₂O₉Ti·2H₂O), polyvinylidene difluoride (PVDF), iron powder (Fe⁰) and tetracycline hydrochloride (C₂₂H₂₄N₂O₈·HCl) and ethylenediaminetetraacetic acid disodium salt (EDTA) were purchased from Sigma-Aldrich Chemical Reagent Co., China, Sinopharm Chemical Reagent Co., China or Shanghai Chemical Reagents Co., China. All chemicals were used as received without further purification.

Preparation of Hf-PMOF. Typically, HfCl₄ (40 mg), benzoic acid (500 mg) and H₂TCPP (30 mg) in 8 mL of DMF were ultrasonically dissolved in a 20 mL Teflon-lined autoclave. The mixture was heated in 120 °C oven for 72 h. After cooling down to room temperature, the Hf-PMOF was separated by centrifugation at 15,000 rpm for 30 min and washed with DMF and acetone, the purple sample was dried under vacuum at 70 °C for 24 h.

Preparation of APF, RF and MPDF resin. Typically, 3-aminophenol (1 mmol) was dispersed in a bottom-rounded flask containing 30 mL of pure water. Then, formaldehyde solution (300 μL) and aqueous ammonia solution (100 μL) were

sequentially added to the solution. The mixture was stirred at 30 °C for 24 h, yielding APF after centrifugation and washing with deionized water (18.25 Ω) and ethanol, the light-yellow sample was dried under vacuum at room temperature for 48 h. Resorcinol and meta phenylenediamine were employed as precursors instead of 3-aminophenol to obtain RF and MPDF resins, respectively.

Preparation of HA-x heterostructure. HA-x was prepared by adding different masses of 3-aminophenol ligands. Specifically, 20 mg of Hf-PMOF was dispersed into a bottom-rounded flask containing 30 mL of water. 3-aminophenol, formaldehyde solution and aqueous ammonia solution were sequentially added into the flask. HA-x ($x = 1, 2, 3, 4$) was prepared by adding 0.1, 0.2, 0.3, and 0.4 mmol 3-aminophenol, respectively. The mixture was stirred at 30 °C for 24 h, yielding HA-x after centrifugation and washing with deionized water (18.25 Ω) and ethanol, the brownish-red sample was dried under vacuum at room temperature for 48 h.

Photocatalytic activity evaluation. The photocatalytic H₂O₂ production experiment was conducted in a 50 mL single-neck flask equipped with a quartz cap. 10 mg of photocatalyst was dispersed in the photochemical reactor with O₂-saturated aqueous solution (50 mL). Utilizing a 300 W xenon lamp to simulate solar light, the solution was exposed to light irradiation. Throughout the reaction process, a continuous flow of oxygen was maintained. Following the initiation of light exposure, the reaction solution was collected at equal time intervals. The H₂O₂ concentration was determined using the potassium titanyl oxalate method. Specifically, 3 mL solution was withdrawn using syringe equipped with 0.22 μm filter, and it was mixed with 1 mL of 0.02 M potassium

titanyl oxalate solution. In consequence, based on the absorbance at 400 nm detected by UV-Vis spectrophotometer, the yields of H₂O₂ can be calculated by the calibration curve (Fig. S1, ESI†).

For the stability test, 25 mg HA-2 photocatalyst was used per test under otherwise identical conditions. Specifically, following each test, the reaction solution was filtered through a sand core micro-filtration to collect the photocatalyst. The filtrate was then analyzed for H₂O₂ concentration. Subsequently, the photocatalyst-loaded microfilter was subjected to vacuum filtration using a 0.22 μm membrane filter. The recovered catalyst was dried in the vacuum oven at 80 °C for 3 h and redispersed in 50 mL deionized water via ultrasonication prior to the next cycle.

Electrochemical measurements. The Mott–Schottky plots, photocurrent response and electrochemical impedance of the catalysts were measured on an electrochemical workstation (CHI660D, CHI Instruments, Shanghai, China). A 395 nm LED was utilized as the light source and 1 M Na₂SO₄ aqueous solution was used as the supporting electrolyte throughout the photocurrent measurements. A platinum wire and Ag/AgCl electrode were used as, counter electrode and reference electrode, respectively. 0.05 g catalyst was dissolved in about 500 μL ethanol with 0.25% Nafion (50 μL). Then, a glass stick was applied to FTO with a layer of high-temperature adhesive tape on the edge, followed by drying in air.

Apparent quantum yield (AQY) efficiency calculation. The AQY of photocatalytic H₂O₂ production was measured in pure water under O₂ atmosphere, the process of

which was consistent with the tests of photocatalytic H₂O₂ production. The AQY of photocatalytic H₂O₂ production was calculated by using the equations:

$$AQY (\%) = \frac{2n_{H_2O_2} \times N_A}{N} \times 100$$

$$N = \frac{E\lambda}{hc}$$

where N_A is Avogadro constant ($6.02 \times 10^{23} \text{ mol}^{-1}$), E is the incident light energy, λ is the wavelength of incident light, h represents the plank constant ($6.626 \times 10^{-34} \text{ J s}$), and c is the speed of light ($3.0 \times 10^8 \text{ m s}^{-1}$).

Characterization methods. The phase structure and composition of the as-prepared photocatalysts were investigated by an X-ray diffractometer (XRD, Panalytical Empyrean Diffractometer, Netherlands) with Cu-K α radiation ($\lambda=0.15418 \text{ nm}$) in the 2θ range from 20° to 80° . Solid-state ^{13}C CP/MAS nuclear magnetic resonance (NMR) spectra were obtained on a Bruker avance III 600 MHz spectrometer. The ^{13}C NMR results were analyzed combined with the prediction tool of NMR software. Field emission scanning electron microscope (FESEM) images were acquired on a HITACHI Regulus 8220 scanning electron microscope operating. The surface morphologies images of samples were characterized using a transmission electron microscopy (TEM, Tecnai G2 F30). The thicknesses of the samples were measured on an atomic force microscope (AFM) using the ScanAsyst in Air scan mode (Bruker Dimension Icon) and the same equipment was used for performing Kelvin probe force microscopy (KPFM). Brunauer-Emmett-Teller (BET) specific surface area value (S_{BET}) was estimated on a three-station full-function multi-purpose gas adsorption instrument

(3Flex, Micrometrics Inc.). The Zeta potentials of samples were obtained on a Zeta potentiostat (Malvern Zetasizer Nano ZS90). The optical performance of different samples was conducted by UV-Vis diffuse reflectance spectroscopy (PerkinElmer Lambda 950) measurements. Photoluminescence (PL) spectroscopy and time-resolved photoluminescence (TRPL) spectra were obtained from a fluorescence lifetime and steady state spectrometer (FLS-980). Fourier-transform infrared (FT-IR) spectra were conducted on a Thermo Scientific Nicolet iS20 infrared spectrophotometer. In situ diffuse reflectance infrared Fourier transformed spectroscopy (DRIFTS) were conducted using the Bruke Tensor II FTIR NEXUS spectrometer. The concentration of intermediates in the oxygen reduction process was monitored by in-situ electron spin resonance (In situ ESR, Bruker EMXplus-9.5/12, DMPO as capture agent) within 10 min. The surface electronic states of Hf-PMOF, APF and HA-2 were measured by using X-ray photoelectron spectroscopy (XPS, SHIMADZU (Kratos)). All the peaks were calibrated with C 1s peak at 284.8 eV to determine the accurate binding energies (± 0.1 eV).

Femtosecond transient absorption (fs-TA) spectroscopy characterization. The *fs-TA* spectroscopy was carried out by using an optical instrument combined a frequency-doubled mode-locked Ti:sapphire femtosecond laser (coherent) and an optical parametric amplifier (OPA) system. The amplified Ti:sapphire femtosecond laser generates seed pulses with a 35 fs pulse width and a repetition rate of 1 kHz. The seed pulses are divided into two distinct beams. The strong beam is sent to the OPA system and provided the 400 nm pump laser pulse, and the other one is focused onto a sapphire

crystal to generate a white light continuum, providing broad band of 420-750 nm UV-Vis probe light. The excitation beam has a low energy of $1 \mu\text{J}/\text{cm}^2$ per pulse to avoid the exciton-exciton and exciton-charge annihilation effects.

In situ diffuse reflectance infrared Fourier transformed spectroscopy (DRIFTS). In situ DRIFTS spectroscopy measurements were applied by using the spectrometer equipped with an in situ diffuse reflectance cell. Before measurement, the powder sample is degassed at 423 K for 4 h. The sample was sweep by N_2 gas to remove impurities for 30 min, and simultaneously water vapor and O_2 were continuous added into the reactor with the sample in the dark. After the adsorption and desorption equilibrium, the container illuminated with 300 W Xe lamp equipped with a 400 nm filter ($\lambda > 400 \text{ nm}$), recorded once every 10 min.

Computational details. Density function theory (DFT) calculations were performed by using the CP2K-2022.1 package. Perdew-Burke-Ernzerh (PBE) of functional was used to describe the system. Unrestricted Kohn-Sham DFT has been used as the electronic structure method in the framework of the Gaussian and plane waves (GPW) way. The Goedecker-Teter-Hutter (GTH) pseudopotentials and Three- ζ molecularly optimized basis sets with two polarization functions (TZV2P-MOLOPT-GTH) have been used for all elements. The Brillouin zone was sampled with gamma points for surface calculation. A plane-wave energy cutoff of 400 Ry ($1\text{Ry} = 13.606 \text{ eV}$) has been employed. The geometries were optimized using the Broyden-Fletcher-Goldfarb-Shanno (BFGS) algorithm. The convergence threshold of density matrix during self-

consistent field (SCF) method was 1×10^{-5} Hartree, and convergence criterion for the forces was set to 4.5×10^{-4} Bohr/Hartree.¹ A vacuum layer of 15 Å was constructed to eliminate interactions between periodic structures of surface models. The van der Waals (vdW) interaction was amended by the DFT-D3 method of Grimme. The Gibbs free energy for intermediates of O₂ photoreduction was calculated as $\Delta G = \Delta E + \Delta E_{ZPE} - T\Delta S$, where the ΔE , ΔE_{ZPE} , and ΔS are electronic energy, zero-point energy, and entropy difference between products and reactants. The zero-point energies of isolated and adsorbed molecules were calculated from the frequency analysis.² The entropies of molecules in the gas phase were taken from the National Institute of Standards and Technology (NIST) database.

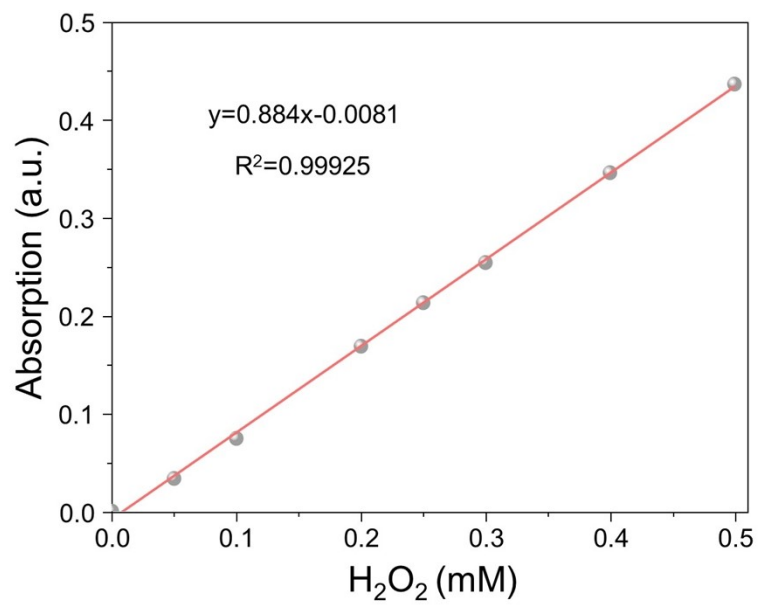


Fig. S1 Standard curve of absorption intensity and H₂O₂ concentration.

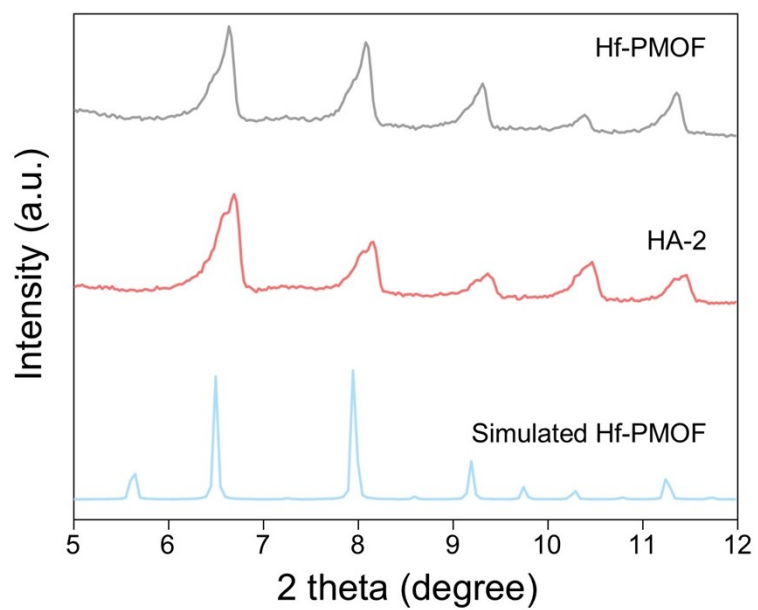


Fig. S2 XRD patterns of Hf-PMOF, HA-2 and simulated Hf-PMOF.

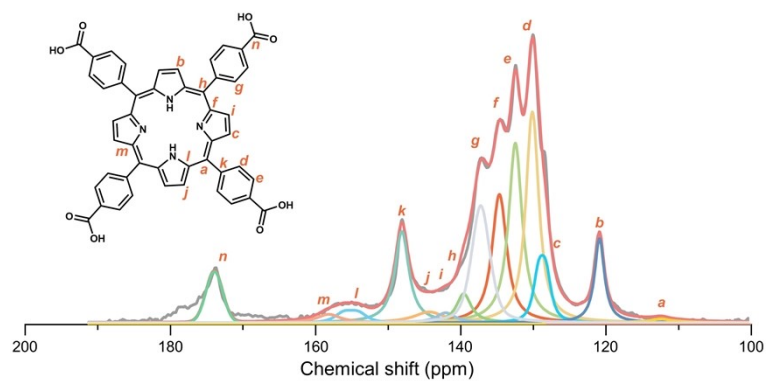


Fig. S3 Solid-state ^{13}C NMR spectrum of Hf-PMOF (inset: corresponding carbon structures in Hf-PMOF).

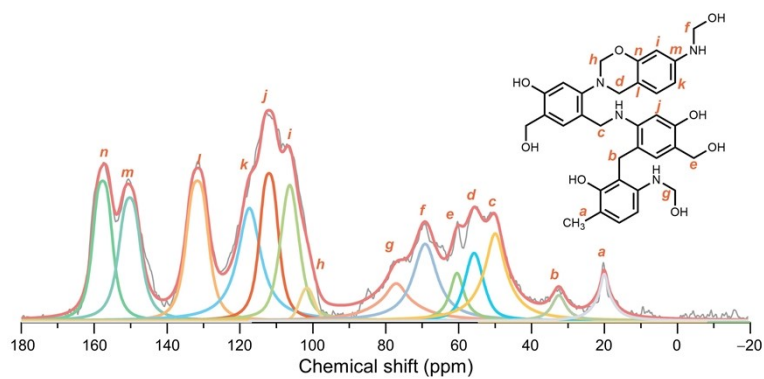


Fig. S4 Solid-state ^{13}C NMR spectrum of APF (inset: corresponding carbon structures in APF).

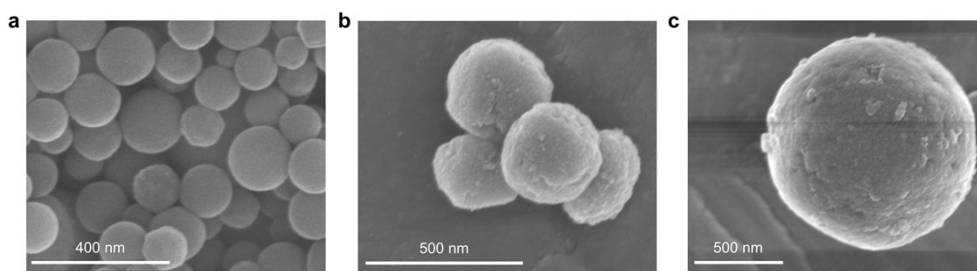


Fig. S5 SEM images of APF (a), Hf-PMOF (b), and HA-2 (c).

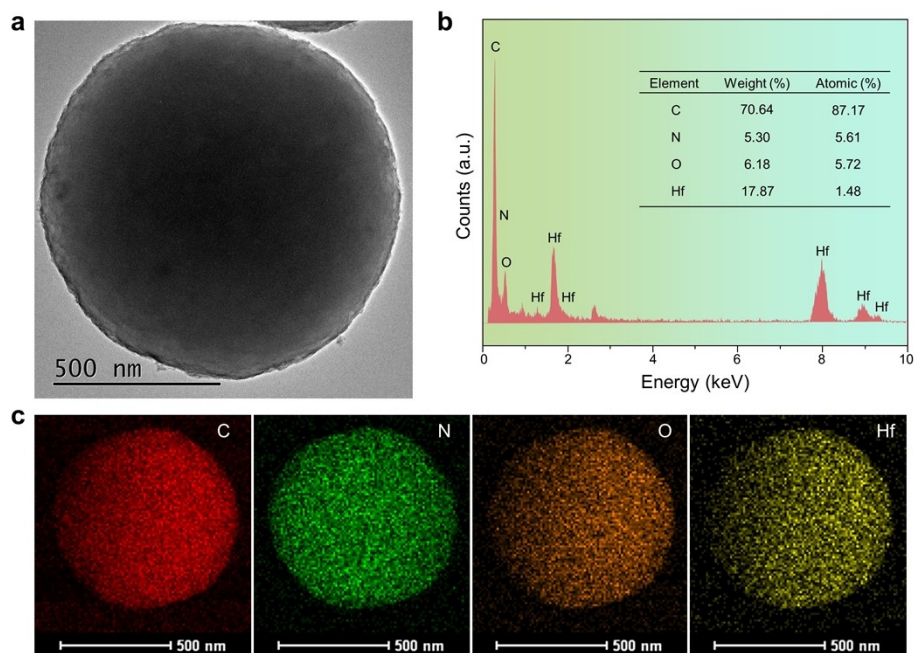


Fig. S6 (a) TEM image of Hf-PMOF. (b) EDS point analysis of Hf-PMOF and the content of each element. (c) TEM-EDS elemental mapping images of Hf-PMOF.

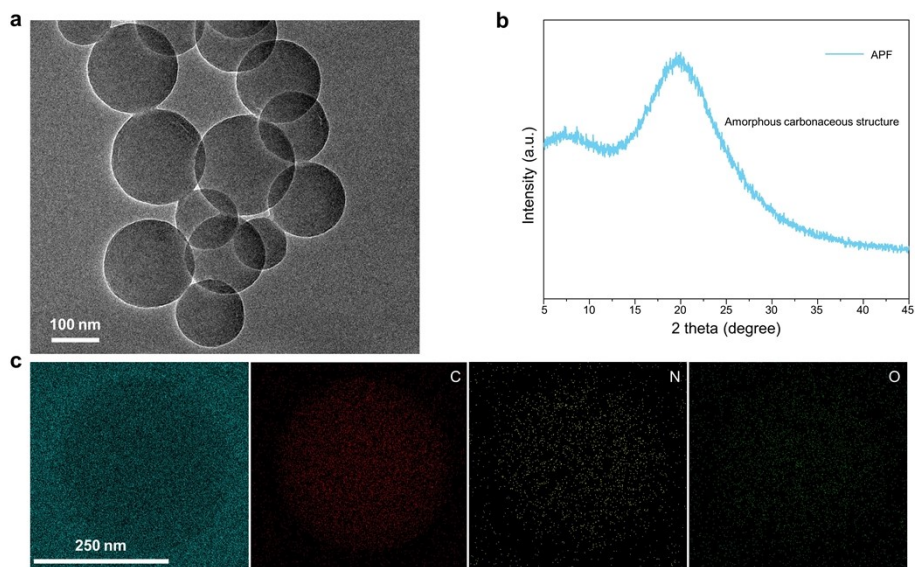


Fig. S7 (a) TEM image of APF. (b) XRD pattern of APF. (c) SEM-EDS elemental mapping images of APF.

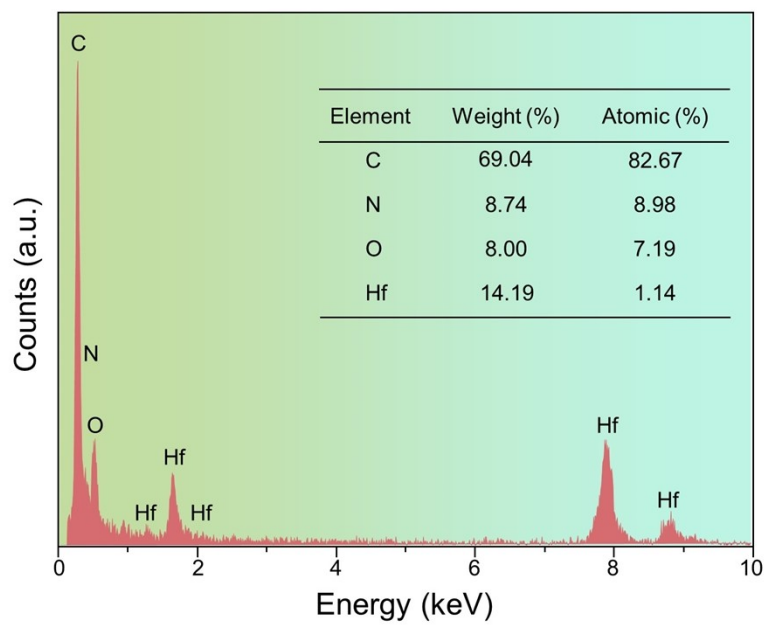


Fig. S8 EDS point analysis of HA-2 and the content of each element.

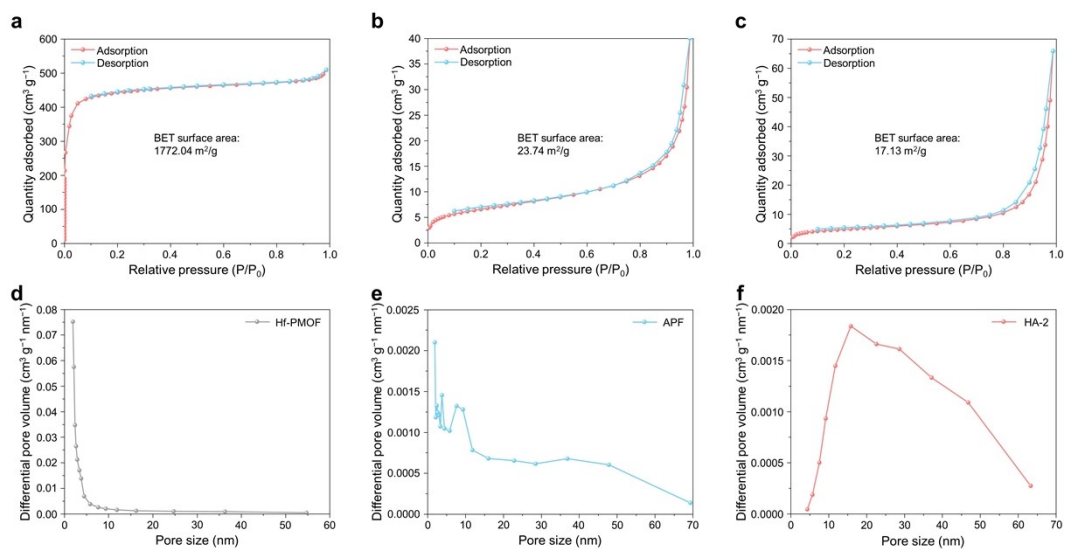


Fig. S9 N_2 adsorption-desorption isotherms of Hf-PMOF (a), APF (b), and HA-2 (c). Pore-size distribution curves of Hf-PMOF (d), APF (e), and HA-2 (f).

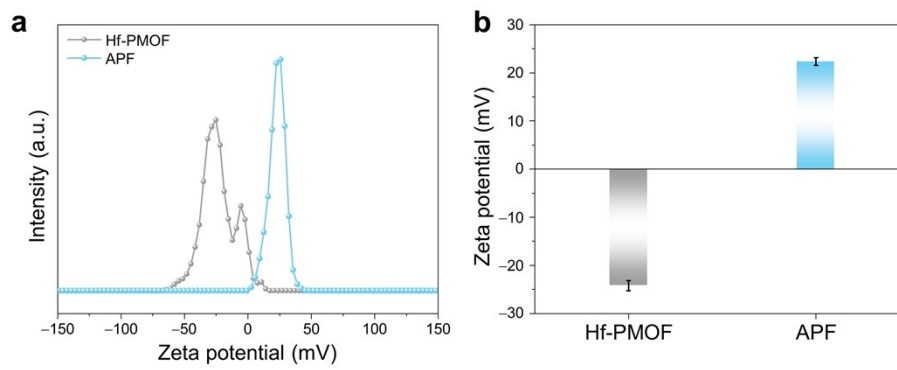


Fig. S10 Zeta potentials of APF and Hf-PMOF.

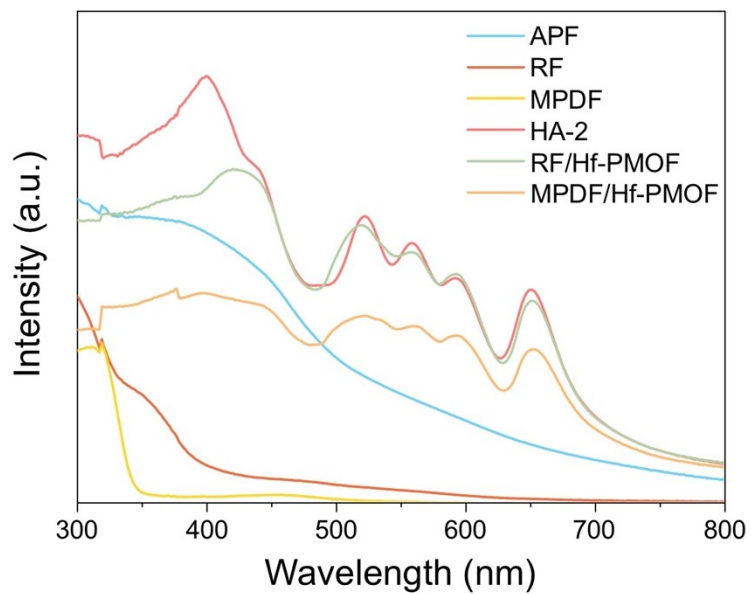


Fig. S11 UV-Vis DRS absorption spectra of phenolic resins and their composites prepared by different precursors.

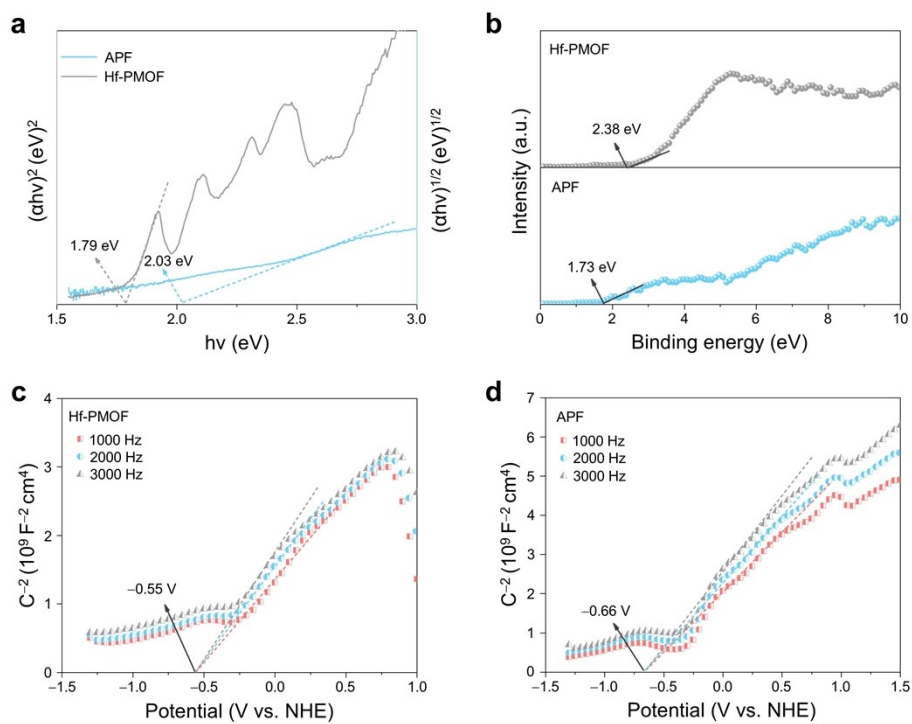


Fig. S12 Kubelka-Munk energy curve plots (a) and valence band-XPS spectra (b) of APF and Hf-PMOF. c,d) Mott-Schottky plots recorded at different frequencies of Hf-PMOF (c) and APF (d).

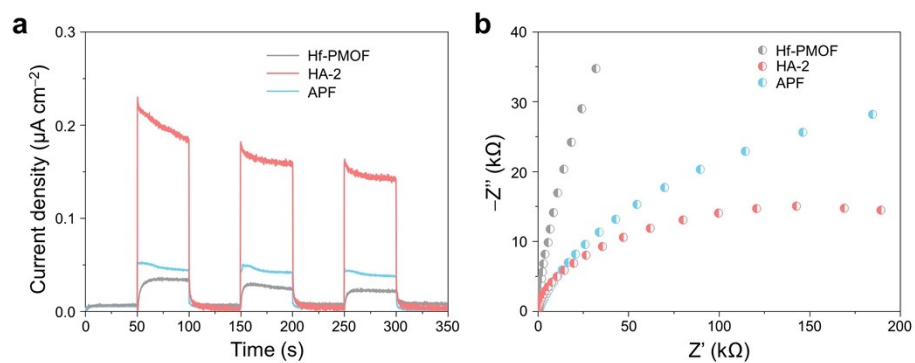


Fig. S13 (a) Transient photocurrent density and (b) electrochemical impedance spectra of APF, Hf-PMOF and HA-2.

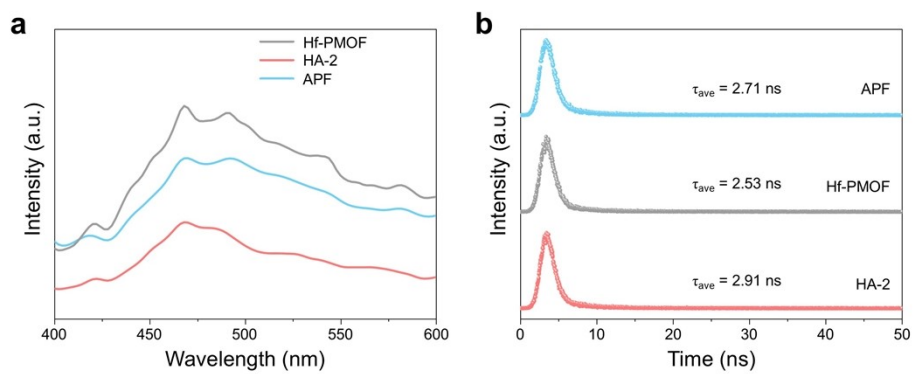


Fig. S14 (a) PL spectra and (b) TRPL spectra of APF, Hf-PMOF and HA-2.

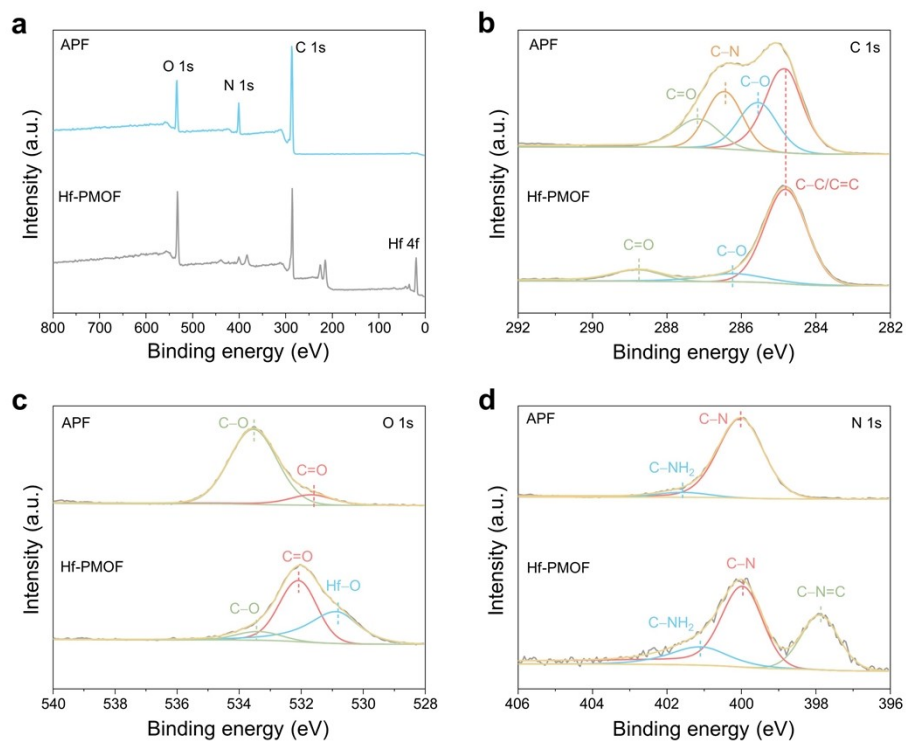


Fig. S15 (a) XPS survey spectra of APF and Hf-PMOF. (b–d) High-resolution C 1s (b), O 1s (c), and N 1s (d) spectra of APF and Hf-PMOF.

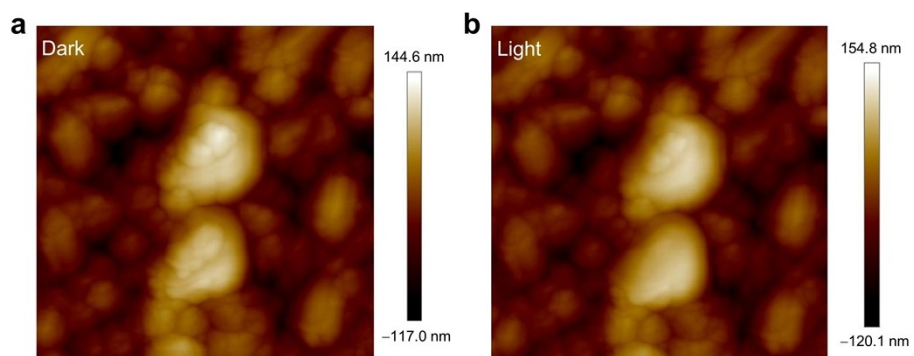


Fig. S16 AFM images of HA-2 under dark conditions (a) and light irradiation (b).

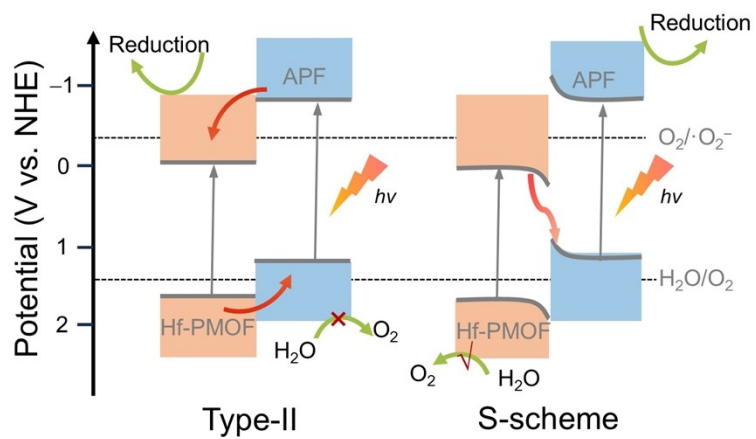


Fig. S17 Schematic illustration of the charge transfer route in type-II heterojunction and S-scheme heterojunction.

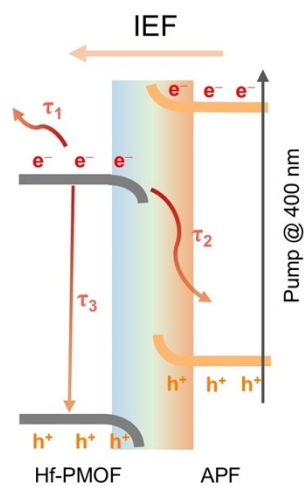


Fig. S18 Schematic illustration of S-scheme photogenerated charge carrier transfer dynamics in HA-2.

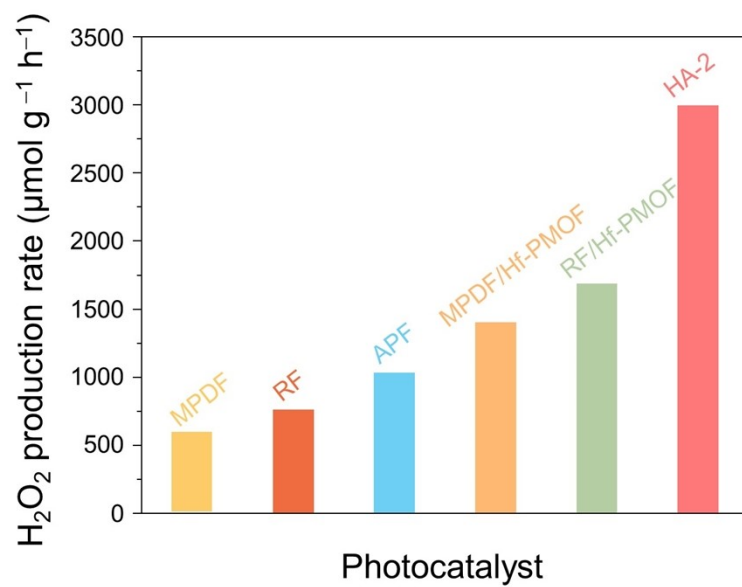


Fig. S19 Photocatalytic performance of phenolic resins and their composites prepared by different precursors.

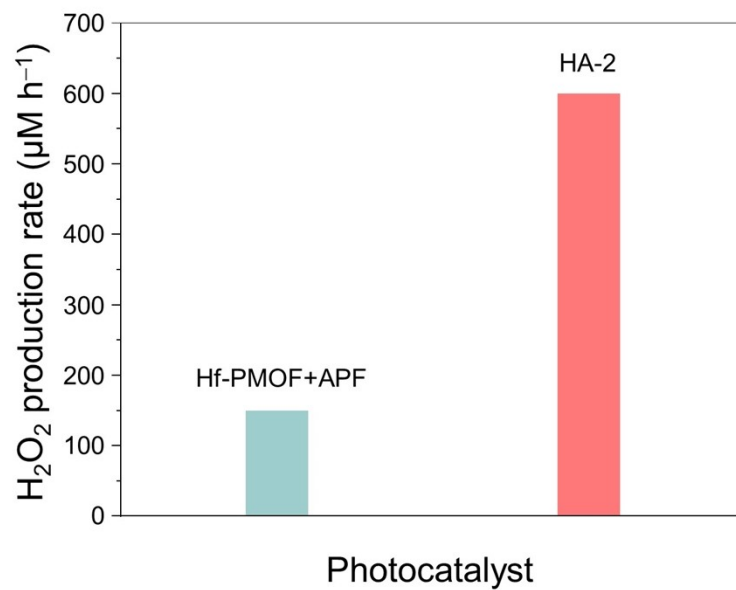


Fig. S20 Photocatalytic performance of the HA-2 heterojunction and its physically mixed counterparts.

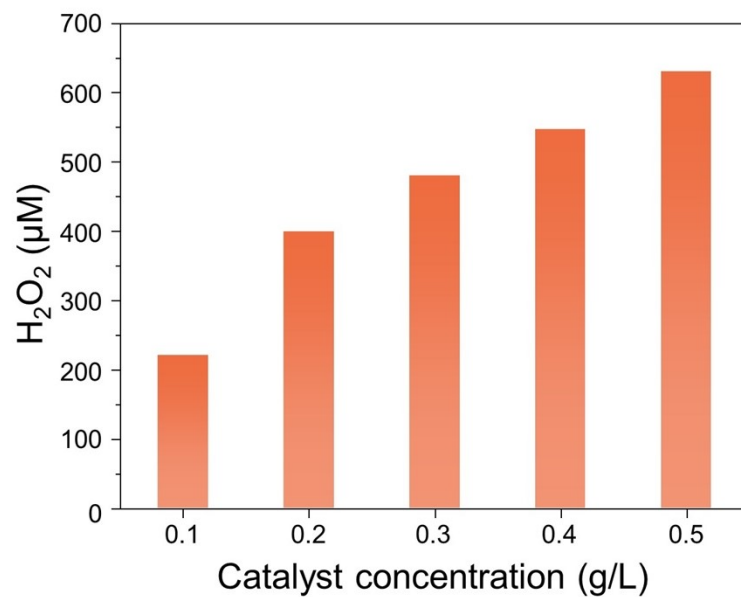


Fig. S21 H₂O₂ yield of HA-2 with different catalyst dosages under visible light irradiation (reaction conditions: reaction duration of 40 min, 50 mL pure water and $\lambda > 400$ nm).

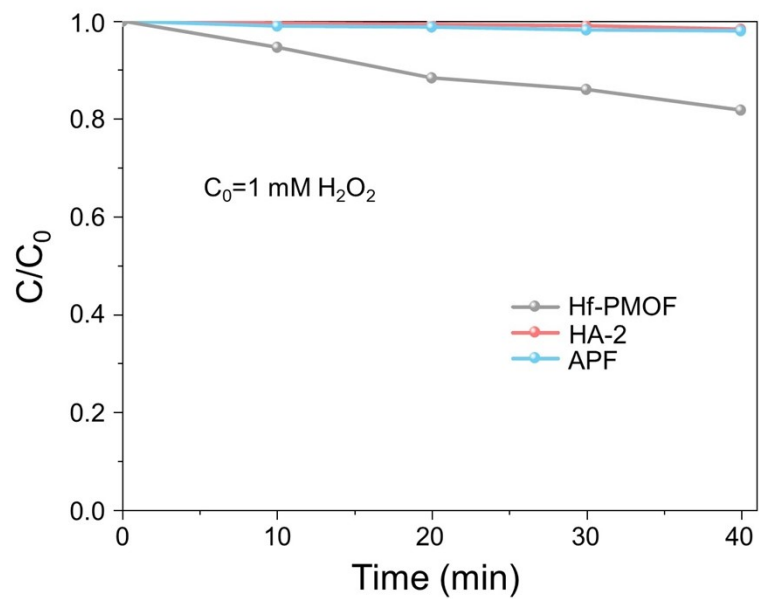


Fig. S22 Decomposition curves of H₂O₂ under light irradiation and Ar atmosphere (initial H₂O₂ concentration: 1 mM).

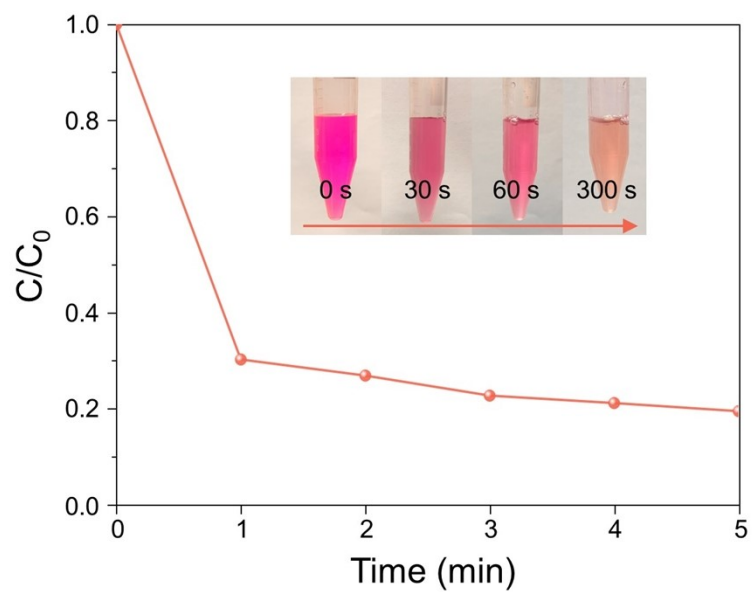


Fig. S23 Fenton degradation of RhB solution (10 mg L^{-1}) with H_2O_2 solution generated by HA-2 under light illumination for 10 h.

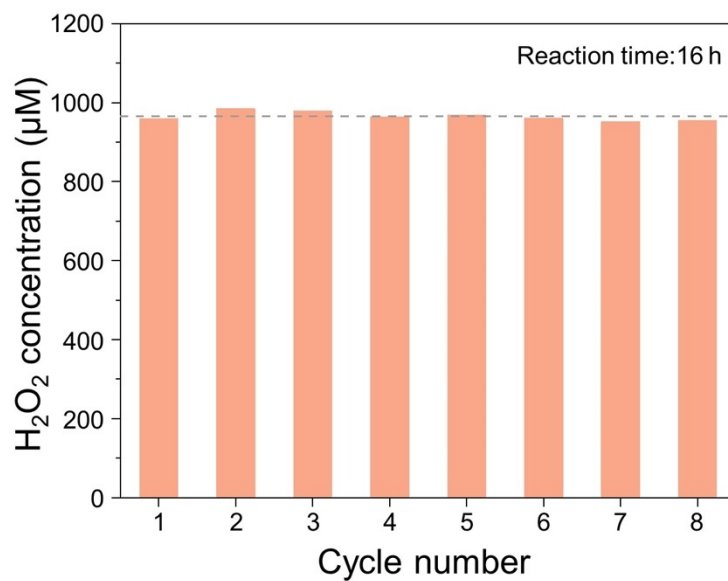


Fig. S24 H₂O₂ evolution recycling stability test of HA-2. The illumination time for each cycle is 2 h and the horizontal dashed line represents the mean values.

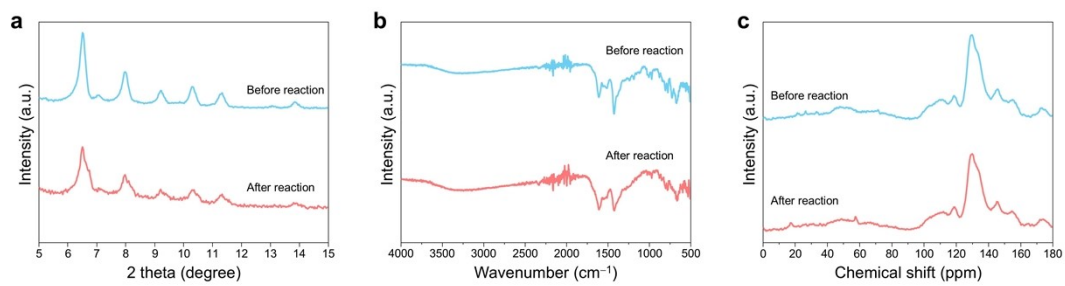


Fig. S25 (a) XRD patterns, (b) FT-IR spectra, and (c) solid-state ¹³C NMR spectra of HA-2 before and after photocatalytic reaction.

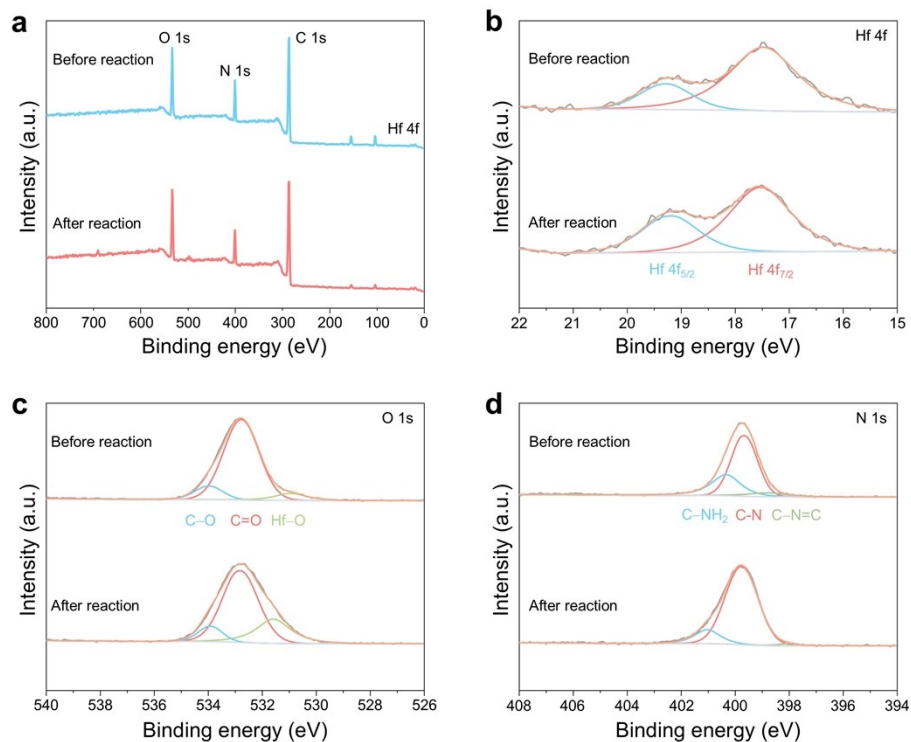


Fig. S26 (a) XPS survey spectra of HA-2 before and after photocatalytic reaction. (b–d) High-resolution Hf 4f (b), O 1s (c), and N 1s (d) XPS spectra of HA-2 before and after photocatalytic reaction.

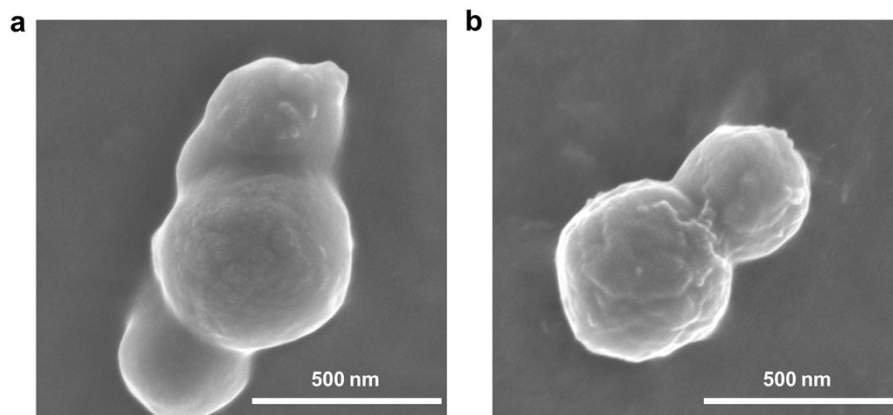


Fig. S27 SEM images before (a) and after photocatalytic reaction (b) of HA-2.

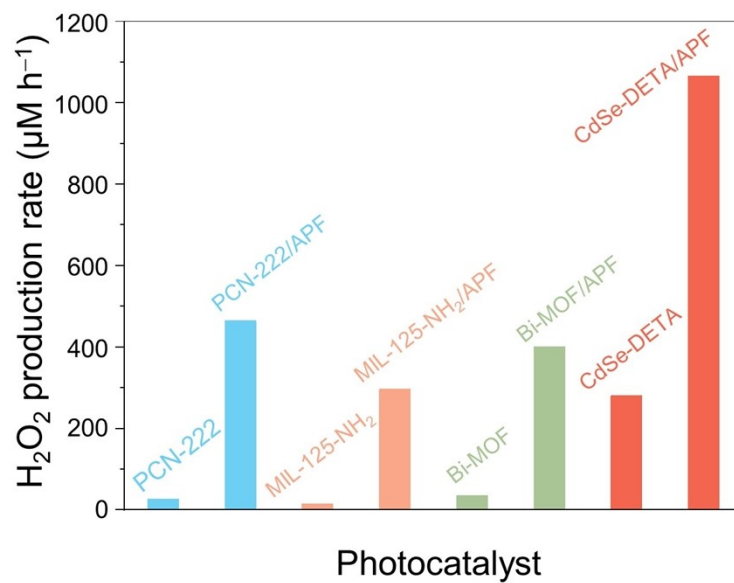


Fig. S28 Photocatalytic performance of PCN-222, MIL-125-NH₂, Bi-MOF, and CdSe-DETA before and after APF resin encapsulation.

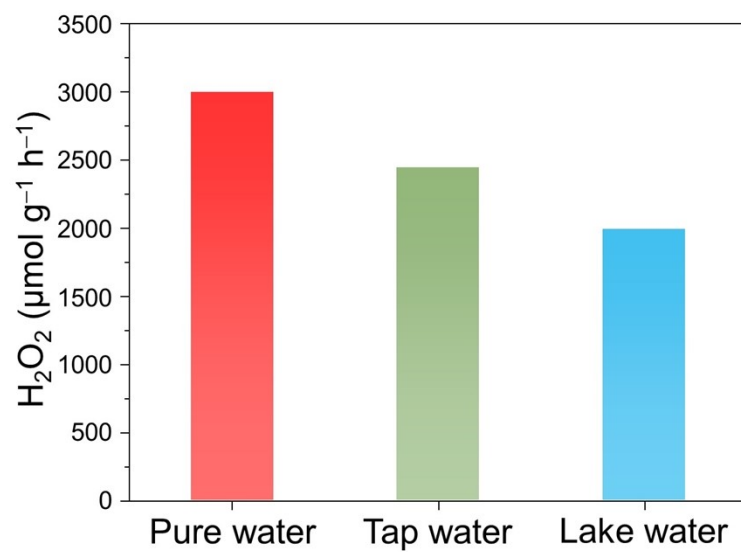


Fig. S29 Comparison of H₂O₂ photosynthesis in pure water, tap water and lake water (reaction conditions: 10 mg catalyst, 50 mL pure water, and $\lambda > 400$ nm).

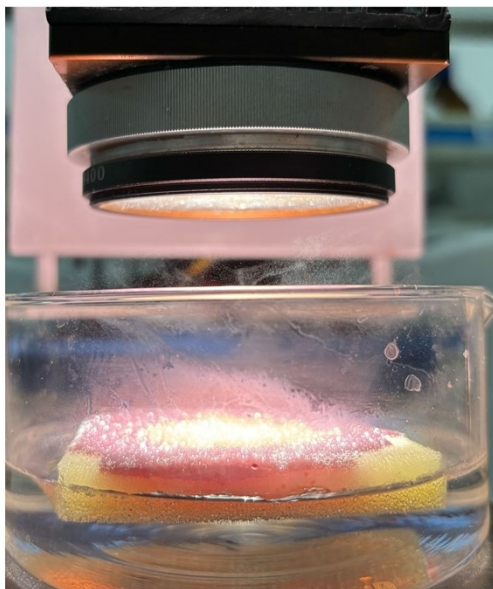


Fig. S30 Optical image of the floatable photocatalytic platform.

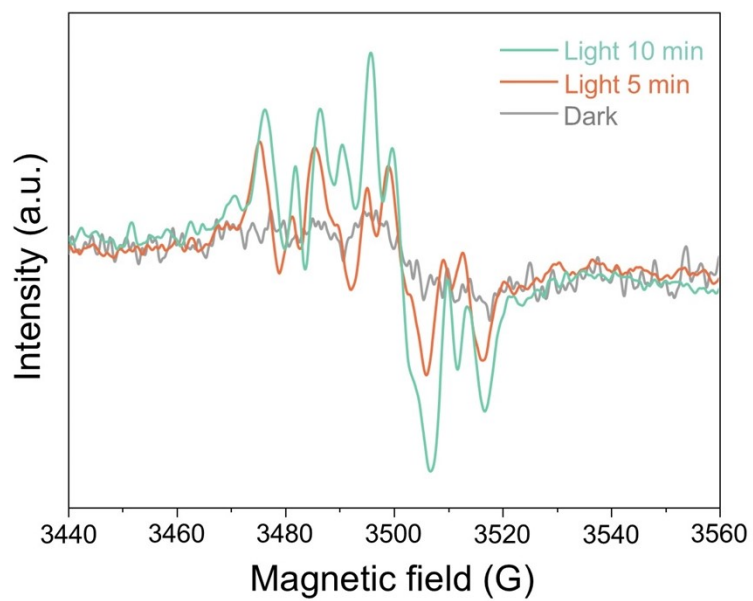


Fig. S31 In situ ESR spectra for HA-2 with different irradiation times under visible light irradiation and O₂ atmosphere.

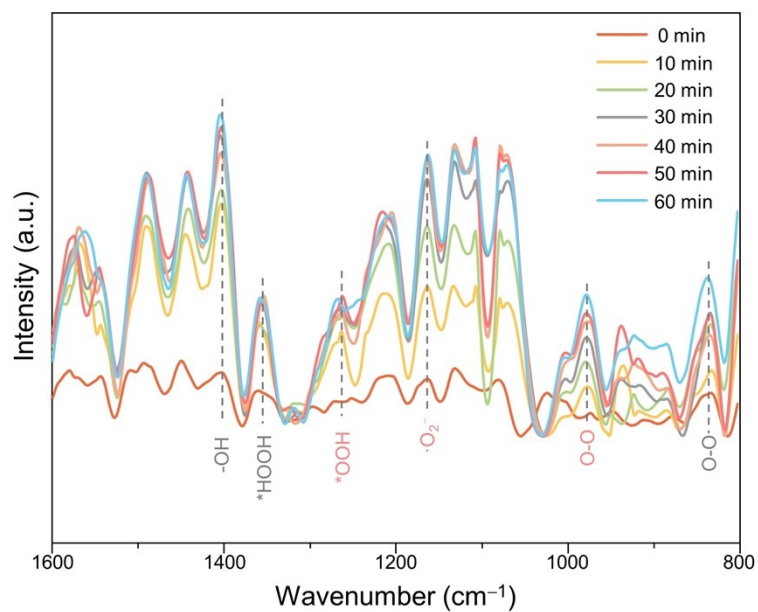


Fig. S32 In situ DRIFTS spectra of HA-2 collected at different photoirradiation times under O₂ and steam environment.

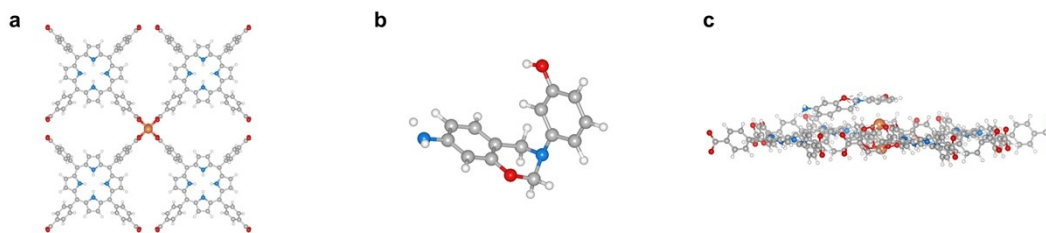


Fig. S33 Optimized structures of Hf-PMOF (a), APF (b), and HA-2 (c).

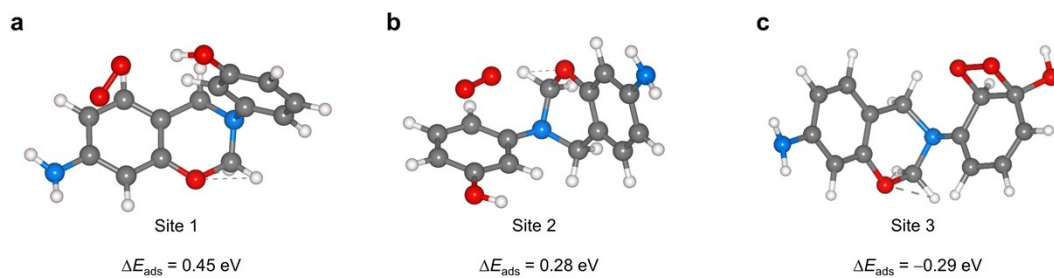


Fig. S34 Optimized O_2 adsorption configurations and calculated adsorption energy (ΔE_{ads}) of O_2 at different sites of APF.

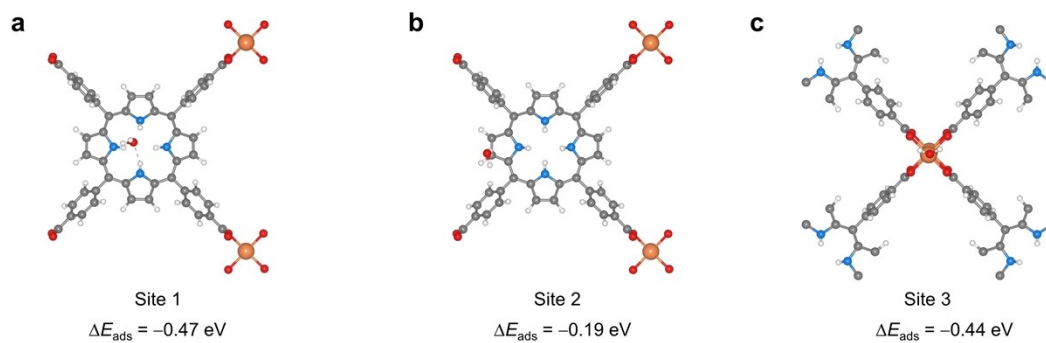


Fig. S35 Optimized H₂O adsorption configurations and calculated adsorption energy (ΔE_{ads}) of H₂O at different sites of Hf-PMOF.

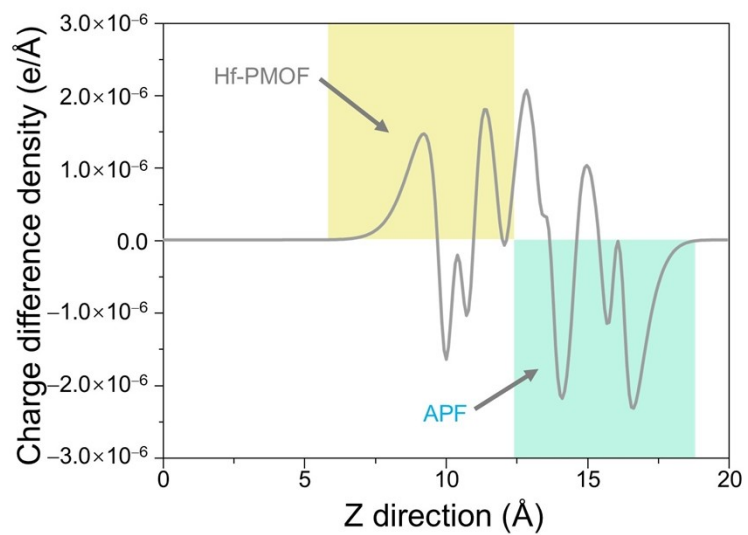


Fig. S36 Planar average potential density curve of HA-2.

Table S1. Fitted results of the fs-TA decay curves of Hf-PMOF, APF, and HA-2 at 585 nm.

| Samples | A_1 | τ_1 (ps) | A_2 | τ_2 (ps) | A_3 | τ_3 (ps) |
|----------------|--------|---------------|--------|---------------|--------|---------------|
| Hf-PMOF | 0.6508 | 43.9 | 0.3492 | 695.5 | - | - |
| APF | 0.1907 | 52.0 | 0.8093 | 788.9 | - | - |
| HA-2 | 0.1554 | 7.0 | 0.6376 | 97.8 | 0.2070 | 1210.0 |

Table S2. Activity comparison of HA-2 photocatalyst with the state-of-the-art porphyrin-based photocatalytic systems for H₂O₂ photosynthesis.

| Catalyst | Reactant | Gas | Light source | Normalized H ₂ O ₂ production rate (μmol g ⁻¹ h ⁻¹) | Normalized H ₂ O ₂ accumulation rate (μM h ⁻¹) | Reference |
|------------------------|---|----------------|--------------------------------|--|--|-----------|
| HA-2 | 10 mg catalyst + 50 mL H ₂ O | O ₂ | 300 W Xenon lamp (λ > 400 nm) | 2995.13 | 599.03 | This work |
| SA-TCPP | 25 mg catalyst + 50 mL H ₂ O, 353 K | O ₂ | 300 W Xenon lamp (420 ± 10 nm) | 1150 | 660 | 3 |
| PCN-222-BA | 20 mg catalyst + 64 mL H ₂ O + 16 mL ethanol | O ₂ | 300 W Xenon lamp (λ > 420 nm) | 148 | 37 | 4 |
| Zn-TCPP/CN | 20 mg catalyst + 50 mL of ethanol aqueous solution (10 vol%) | O ₂ | 300 W Xenon lamp | 591.88 | 355.13 | 5 |
| Al-TCPP4-TBAPy6 | 5 mg catalyst + 5 mL H ₂ O | O ₂ | 300 W Xenon Lamp (λ > 420 nm) | 127 | 127 | 6 |
| TCFPP-TPD | 10 mg catalyst + 20 mL H ₂ O | O ₂ | 300 W Xenon Lamp (λ > 420 nm) | 1180 | 590 | 7 |
| NMA-Ga5%-L30 | 5 mg catalyst + 30 mL H ₂ O | O ₂ | 300 W Xenon Lamp (λ > 420 nm) | 268.7 | 44.78 | 8 |
| Au-Co-TCPP | 5 mg catalyst + 5 mL H ₂ O | O ₂ | 300 W Xenon Lamp (λ > 420 nm) | 235.93 | 235.93 | 9 |
| Al ^{III} TCPP | 1 g L ⁻¹ H ₂ O/CH ₃ CN (1/9 v/v) | O ₂ | LED light (420 nm) | 5 | 5 | 10 |

Table S3. Comparison of PHP performance of HA-2 with the state-of-the-art materials.

| Catalyst | Reactant | Gas | Light source | Normalized H ₂ O ₂ production rate (μmol g ⁻¹ h ⁻¹) | Normalized H ₂ O ₂ accumulation rate (μM h ⁻¹) | Reference |
|---|---|----------------|---|--|--|-----------|
| HA-2 | 10 mg catalyst + 50 mL H ₂ O | O ₂ | 300 W Xenon lamp (λ > 400 nm) | 2995.13 | 599.03 | This work |
| APFac | 10 mg catalyst + 50 mL H ₂ O | O ₂ | 300 W Xenon lamp (λ > 420 nm) | 1123 | 224.6 | 11 |
| Ni _{SAPs} -PuCN | 30 mg catalyst + 30 mL H ₂ O | O ₂ | 300 W Xenon lamp (λ > 420 nm) | 342.2 | 342.2 | 12 |
| QAP ₂ | 10 mg catalyst + 50 mL H ₂ O | Air | 300 W Xenon lamp (λ > 420 nm) | 380 | 76 | 13 |
| ME250 | 10 mg catalyst + 50 mL H ₂ O | Air | 300 W Xenon lamp (λ > 420 nm) | 330 | 66 | 14 |
| CN-PDA | 30 mg catalyst + 20 mL H ₂ O | Air | 400 nm < λ < 780 nm | 495.2 | 742.8 | 15 |
| Co ₁₄ (L-CH ₃) ₂₄ | 5 mg catalyst + 10 mL H ₂ O | O ₂ | 300 W Xenon lamp (300 nm < λ < 1100 nm) | 146.60 | 73.3 | 16 |
| COF-TfpBpy | 5 mg catalyst + 10 mL H ₂ O | Air | 300 W Xenon lamp (300 nm < λ < 1100 nm) | 2084 | 1042 | 17 |

| | | | | | | |
|--|--|----------------|---|--------|---------|----|
| RF523 | 50 mg catalyst + 30 mL H ₂ O | O ₂ | 300 W Xenon lamp ($\lambda >$ 420 nm) | 51.6 | 86 | 18 |
| Nv- C \equiv N- CN | 20 mg catalyst + 20 mL H ₂ O | O ₂ | AM 1.5G | 323 | 323 | 19 |
| ZnIn ₂ S ₄ @ BiVO ₄ | 10 mg catalyst + 30 mL H ₂ O | O ₂ | 300 W Xenon lamp (400 nm < λ < 1000 nm) | 1800 | 600 | 20 |
| RF/P3H T-1.0 | 50 mg catalyst + 30 mL H ₂ O | O ₂ | 300 W Xenon lamp | 233.2 | 388.67 | 21 |
| RF- DHAQ-2 | 10 mg catalyst + 50 mL H ₂ O | O ₂ | 300 W Xenon lamp | 1820 | 364 | 22 |
| CNNT- Al | catalyst + H ₂ O (1 g L ⁻¹) | O ₂ | 300 W Xenon Lamp | 1410.2 | 1410.2 | 23 |
| QP- HPTP- COF | 30 mg catalyst + 10 mL H ₂ O | O ₂ | 300 W Xenon Lamp | 4388 | 13164 | 24 |
| EA-260 | 10 mg catalyst + 15 mL H ₂ O | Air | Visible light (420 nm \leq λ \leq 700 nm) | 2884.7 | 1923.13 | 25 |

Table S4. Formation energy after structural optimization of Hf-PMOF, APF, and HA-2.

| Structure | Hf-PMOF | APF | HA-2 |
|-------------|------------|------------|------------|
| Energy (eV) | -4614.9352 | -1440.9051 | -6057.2059 |

References

- 1 T. Lu and F. Chen, *J. Comput. Chem.*, 2012, **33**, 580–592.
- 2 T. Lu and Q. Chen, *Comput. Theor. Chem.*, 2021, **1200**, 113249.
- 3 Y. Zhang, C. Pan, G. Bian, J. Xu, Y. Dong, Y. Zhang, Y. Lou, W. Liu and Y. Zhu, *Nat. Energy*, 2023, **8**, 361–371.
- 4 L. Li, X. Wang, H. X. Liu, S. S. Xia, Z. Chen and J. Ye, *J. Catal.*, 2024, **429**, 115249.
- 5 Y. Xia, B. Zhu, X. Qin, W. Ho and J. Yu, *Chem. Eng. J.*, 2023, **467**, 143528.
- 6 Y. Kondo, K. Hino, Y. Kuwahara, K. Mori and H. Yamashita, *J. Mater. Chem. A*, 2023, **11**, 9530.
- 7 R. Zhang, H. Zhao, C. Pan, J. Zhang, L. Jian, X. Sun, R. Ji, J. Li, Y. Dong and Y. Zhu, *New J. Chem.*, 2024, **48**, 3316.
- 8 S.-S. Xia, L. Li, C. Bao, J. Wu, C. Li, X. Wang, J. Gao, J. Hu, X. Wang and Z. Chen, *J. Catal.*, 2024, **433**, 115488.
- 9 Q. Xue, Z. Wang, S. Han, Y. Liu, X. Dou, Y. Li, H. Zhu and X. Yuan, *J. Mater. Chem. A*, 2022, **10**, 8371.
- 10 F. Kuttassery, S. Sagawa, S. Mathew, Y. Nabetani, A. Iwase, A. Kudo, H. Tachibana and H. Inoue, *ACS Appl. Energy Mater.*, 2019, **2**, 8045.
- 11 X. Wang, X. Yang, C. Zhao, Y. Pi, X. Li, Z. Jia, S. Zhou, J. Zhao, L. Wu and J. Liu, *Angew. Chem. Int. Ed.*, 2023, **62**, e202302829.
- 12 X. Zhang, H. Su, P. Cui, Y. Cao, Z. Teng, Q. Zhang, Y. Wang, Y. Feng, R. Feng, J. Hou, X. Zhou, P. Ma, H. Hu, K. Wang, C. Wang, L. Gan, Y. Zhao, Q. Liu, T. Zhang and K. Zheng, *Nat. Commun.*, 2023, **14**, 7115.
- 13 B. Sheng, Y. Xie, Q. Zhao, H. Sheng and J. Zhao, *Energy Environ. Sci.* 2023, **16**, 4612-4619.
- 14 D. Yao, W. Miao, C. Chu, Z. Chen, H. Qin and S. Mao, *Chem. Eng. J.*, 2023, **467**, 143550.
- 15 Y. Deng, W. Liu, R. Xu, R. Gao, N. Huang, Y. Zheng, Y. Huang, H. Li, X. Y. Kong and L. Ye, *Angew. Chem. Int. Ed.*, 2024, **63**, e202319216.
- 16 J. Lu, J. Liu, L. Dong, J. Lin, F. Yu, J. Liu and Y. Lan, *Angew. Chem. Int. Ed.*, 2023, **62**, e202308505.
- 17 M. Kou, Y. Wang, Y. Xu, L. Ye, Y. Huang, B. Jia, H. Li, J. Ren, Y. Deng, J. Chen, Y. Zhou, K. Lei, L. Wang, W. Liu, H. Huang and T. Ma, *Angew. Chem. Int. Ed.*, 2022, **61**, e202200413.
- 18 Y. Shiraishi, T. Takii, T. Hagi, S. Mori, Y. Kofuji, Y. Kitagawa, S. Tanaka, S. Ichikawa and T. Hirai, *Nat. Mater.*, 2019, **18**, 985-993.
- 19 X. Zhang, P. Ma, C. Wang, L. Gan, X. Chen, P. Zhang, Y. Wang, H. Li, L. Wang, X. Zhou and K. Zheng, *Energy Environ. Sci.*, 2022, **15**, 830-842.
- 20 M. Gu, Y. Yang, L. Zhang, B. Zhu, G. Liang and J. Yu, *Appl. Catal. B: Environ.*, 2023, **324**, 122227.
- 21 Y. Shiraishi, M. Matsumoto, S. Ichikawa, S. Tanaka and T. Hirai, *J. Am. Chem. Soc.*, 2021, **143**, 12590-12599.
- 22 C. Zhao, X. Wang, Y. Yin, W. Tian, G. Zeng, H. Li, S. Ye, L. Wu and J. Liu, *Angew. Chem. Int. Ed.*, 2023, **62**, e202218318.
- 23 H. Tan, P. Zhou, M. Liu, Y. Gu, W. Chen, H. Guo, J. Zhang, K. Yin, Y. Zhou, C. Shang, Q. Zhang, L. Gu, N. Zhang, J. Ma, Z. Zheng, M. Luo and S. Guo, *J. Am. Chem. Soc.*, 2024, **146**, 31950-31960.
- 24 J. Cheng, Y. Wu, W. Zhang, L. Wang, X. Wu and H. Xu, *Adv. Mater.*, 2024, **36**, 2410247.
- 25 T. He, H. Tang, J. Wu, J. Wang, M. Zhang, C. Lu, H. Huang, J. Zhong, T. Cheng, Y. Liu and Z.

Kang, *Nat. Commun.*, 2024, **15**, 7833.